Editors' Suggestion | Featured in Physics

Minimal Design of the Elephant Trunk as an Active Filament

Bartosz Kaczmarski, Sophie Leanza, Renee Zhao, and Ellen Kuhl
Department of Mechanical Engineering, Stanford University, Stanford, California 94305, USA

Derek E. Moulton and Alain Goriely*
Mathematical Institute, University of Oxford, Oxford, United Kingdom

(Received 5 November 2023; accepted 22 April 2024; published 14 June 2024)

One of the key problems in active materials is the control of shape through actuation. A fascinating example of such control is the elephant trunk, a long, muscular, and extremely dexterous organ with multiple vital functions. The elephant trunk is an object of fascination for biologists, physicists, and children alike. Its versatility relies on the intricate interplay of multiple unique physical mechanisms and biological design principles. Here, we explore these principles using the theory of active filaments and build, theoretically, computationally, and experimentally, a minimal model that explains and accomplishes some of the spectacular features of the elephant trunk.

DOI: 10.1103/PhysRevLett.132.248402

Introduction.—In nature and engineering, one of the main tasks of active filamentary structures is to explore their surroundings. The simplest problem for the activation of slender structures is curvature generation, a well-understood phenomenon studied by Timoshenko a century ago in the context of bimetallic strips [1]. In Timoshenko's initial setting, curvature changes only generate planar shapes. A more involved problem is the generation of torsion which, through curvature coupling, allows for arbitrary three-dimensional shapes as found in plants [2], but also in the octopus arms and elephant trunks [3]. Here, we take inspiration from the elephant trunk as a design paradigm to couple curvature, twist, and torsion, and create a minimal activation model using three uniform actuators.

The elephant trunk is an elongated, muscular, and highly flexible proboscis made of specialized muscles, fascia, and skin; it represents a unique adaptation of the upper lip and the nose; see Fig. 1. It is made of 17 major muscle groups, eight on each side and one for the nasal cavity, with more than 90 000 muscle fascicles controlled by 50 000–60 000 facial nucleus neurons, which together give it its exceptional strength and versatility of movement [4–6].

Unsurprisingly, the biomechanics of the elephant trunk have attracted the attention of many scientists [9,10] with the ultimate goal of understanding and replicating some of its functions [11]. Yet, some of the basic principles of the trunk have been overlooked. Here, in contrast to most previous studies that use a great number of segmented actuators to replicate function [11–13], we aim to unravel

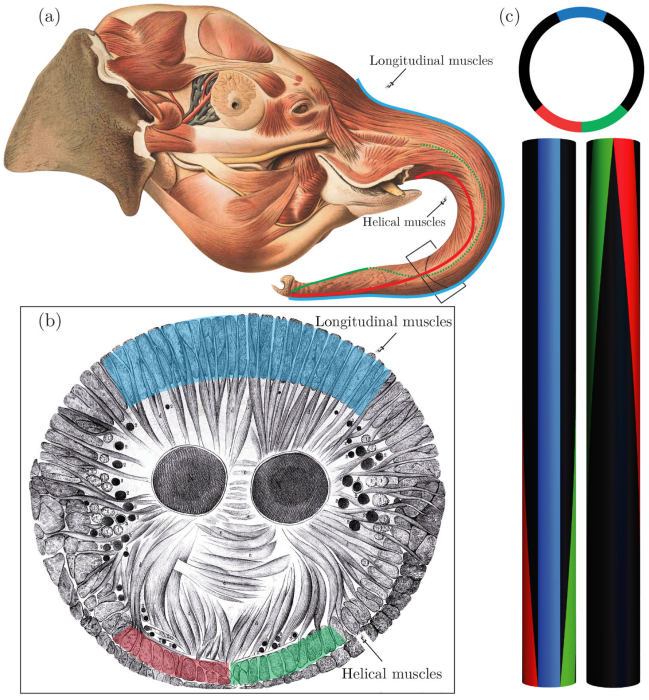

FIG. 1. Muscular architecture within the elephant trunk. (a) Skinned elephant trunk with longitudinal muscles on the dorsal side and helical muscles wrapping along the length on the ventral side [7]. (b) Cross section of a trunk by Cuvier (1850) with longitudinal (blue), helical (red, green), and radial muscles around the two nasal cavities [8]. (c) Minimal model of a trunk with three muscular bundles.

important properties of the trunk by considering an ideal and simplified, single-segment trunk representation with a *minimum number* of actuators that still reproduces some of its key functions. In other words, we seek to reduce the architectural complexities of the elephant trunk anatomy to a *minimal design* that captures only its primary deformation mechanisms. Toward this goal, we show that simple physical models of active materials can help improve our understanding of these spectacular structures, and inspire future design approaches in pursuit of minimal complexity, maximal compactness, and remarkable control versatility.

Inspired by the muscular architecture of the trunk, we propose a minimal model of three actuators and investigate its control capabilities. In particular, we study the design space of our idealized trunk and identify the fundamental trade-off between some desirable properties. We also explore the complex mechanistic interactions of the longitudinal and helical muscle contractions that generate a remarkably rich configuration space with nonuniform curvature, twist, and torsion. Finally, we validate our model predictions experimentally using liquid crystal elastomer actuators, and compare minimal design deformations with the shapes of a moving elephant trunk recorded by Dagenais *et al.* [3].

Model setup.—Despite its massive size, the elephant trunk can be modeled as a slender biological filament that deforms through muscular activation of longitudinal, radial, and helical muscles (Fig. 1). To model the deformation induced by local fiber contraction, we adopt the active filament theory [14–16], which describes a general three-dimensional tubular structure equipped with an arbitrary fiber activation tensor $\mathbf{G}$ dictated by the local orientation of the muscle fibers throughout the continuum. Assuming that initially the trunk is straight, we can write any deformation as $\boldsymbol{\chi} = \boldsymbol{r} + \sum_{i=1}^{3} \varepsilon e_i \mathbf{d}_i$ [17], where $\boldsymbol{r}(Z)$ is the centerline of the deformed tubular structure with respect to the arc length Z of the initial structure, such that $\boldsymbol{r}' = \zeta \mathbf{d}_3$, where ζ is the centerline stretch, εe_i are the cross-sectional reactive strains with ε being the inverse of the slenderness ratio (the length L divided by a characteristic radius), and $\{\mathbf{d}_1, \mathbf{d}_2, \mathbf{d}_3\}$ form an orthonormal basis that defines the orientation of each cross section so that $\mathbf{d}_i' = \zeta \mathbf{u} \times \mathbf{d}_i$, where $\mathbf{u} = \sum \mathsf{u}_i \mathbf{d}_i$ is the Darboux vector specifying the filament's three curvatures. To model activation, we decompose the deformation gradient [18], $\mathbf{F} = \mathrm{Grad}\boldsymbol{\chi} = \mathbf{A}\,\mathbf{G}$, into an elastic contribution $\mathbf{A}$ and the activation $\mathbf{G}$. Using a systematic energy minimization procedure, we then obtain the intrinsic curvatures $\hat{\mathsf{u}}_1, \hat{\mathsf{u}}_2, \hat{\mathsf{u}}_3$, and the extension $\hat{\zeta}$ of the trunk in the absence of external loads by integrating the contribution of each fiber contraction over the cross section [16]. In the case of a ring of helical fibers with helical angle α and radii R_1 and R_0 (see Fig. 2), the curvatures are

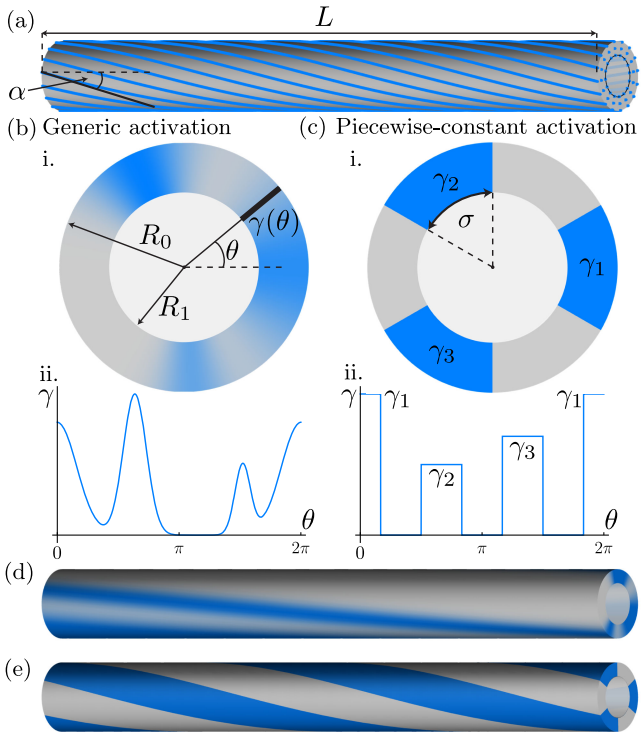

FIG. 2. Active filament model. (a) Filament with embedded helically arranged fibers. (b),(d) Realistic continuous muscle activation $\gamma(\theta)$. (c),(e) Idealized discrete piecewise constant activation with $N = 3$ actuators.

$$\hat{\mathsf{u}}_1(Z) = -\frac{4}{3R_0^4} A\delta_1 \sin\left(\varphi - \frac{Z}{R_0}\tan\alpha\right),$$
$$\hat{\mathsf{u}}_2(Z) = -\frac{4}{3R_0^4} A\delta_2 \cos\left(\varphi - \frac{Z}{R_0}\tan\alpha\right),$$
$$\hat{\mathsf{u}}_3(Z) = \frac{2}{R_0^4}\delta_3 a_0, \qquad \hat{\zeta} = 1 + \frac{1}{2R_0^2}\delta_0 a_0,$$

where δ_i are functions of the filament geometry, fiber architecture, and mechanical properties; see Supplemental Material (SM) [19]. For a given periodic muscle activation function $\gamma = \gamma(\theta)$, A, φ, a_0 are

$$a_1 = \frac{1}{\pi}\int_0^{2\pi} \gamma(\theta)\cos\theta \mathrm{d}\theta, \qquad b_1 = \frac{1}{\pi}\int_0^{2\pi} \gamma(\theta)\sin\theta \mathrm{d}\theta,$$
$$a_0 = \frac{1}{\pi}\int_0^{2\pi} \gamma(\theta)\mathrm{d}\theta, \qquad A = \sqrt{a_1^2 + b_1^2}, \qquad \tan(\varphi) = -\frac{b_1}{a_1}.$$

The γ function describes the distribution of fibrillar prestrain in the cross section in terms of the angle θ [Fig. 2(b)]. It stems from a restriction on the arbitrarily inhomogeneous form of the activation tensor $\mathbf{G}$, where an activation pattern given by $\gamma(\theta)$ follows the fiber architecture according to its helicity [Fig. 2(d)]; see SM for further details. We further restrict our attention to discrete muscle fiber bundles with inputs $\gamma_1, \ldots, \gamma_N$ and angular

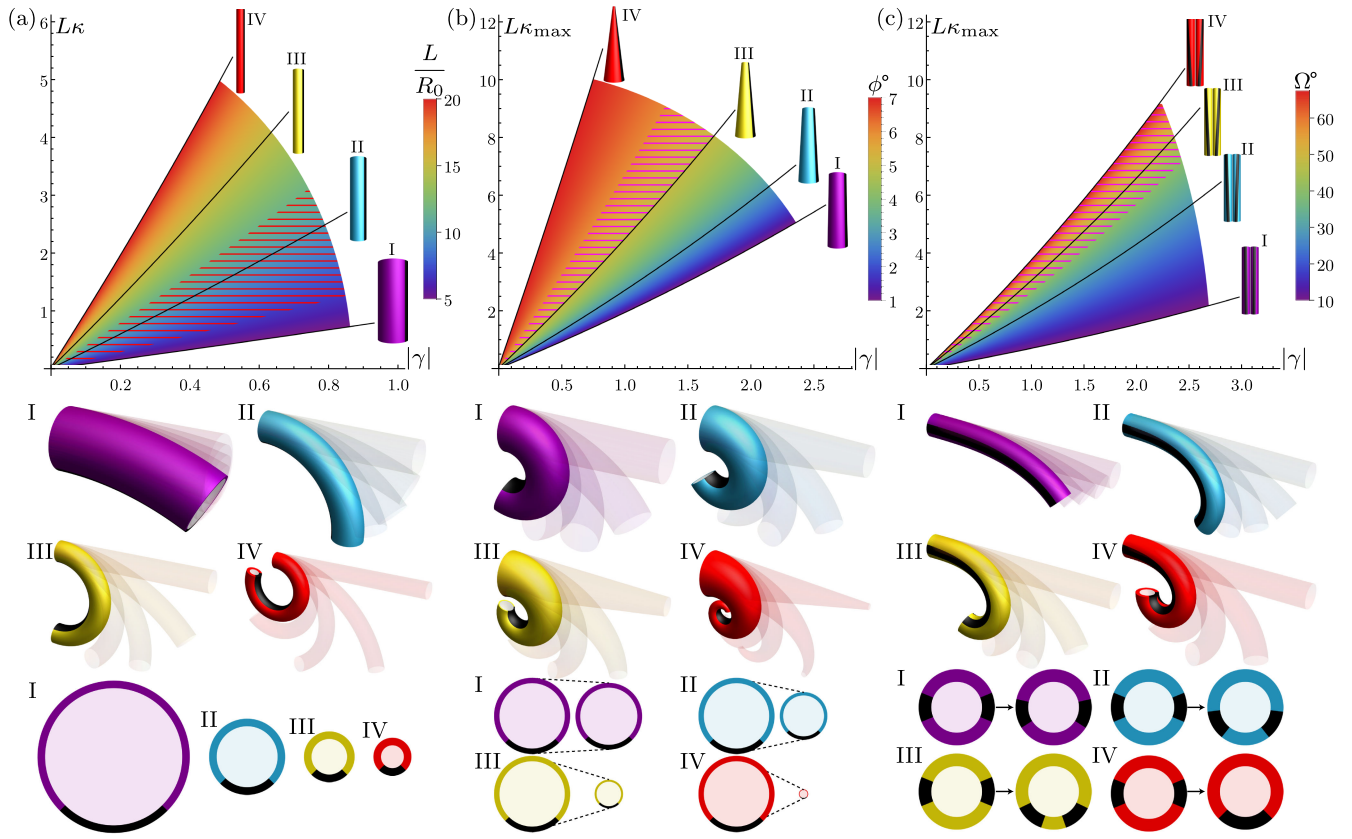

FIG. 3. Design space of the elephant trunk: slenderness, tapering, and fiber helicity. Deformations I, II, III, IV, and their respective curvature-activation curves for (a) varied slenderness ($S_r = 5$, 10, 15, 20, $\gamma = -0.6$) with a single longitudinal bundle ($\sigma = 90°$); (b) varied tapering angle ($\phi = 1°, 3°, 5°, 7°, \gamma = -2.5$) for the same single bundle; and (c) varied helicity ($\Omega \approx 10.0°, 29.2°, 48.3°, 67.5°$, $\gamma = -3$, $\sigma = 45°$ in both bundles) for two symmetrically arranged, equally activated helical fiber bundles. Dashed regions highlight physiological ranges $S_r \in [6.7, 11.7]$, and $\phi \in [5°, 6°]$ for the elephant trunk, and for Ω far from the longitudinal case. Young's modulus is constant, Poisson's ratio is $\nu = 1/2$, and $R_0 - R_1 = L/50$ at $Z = 0$.

extents defined by the parameter σ, as shown in Figs. 2(c) and 2(e).

Design principles.—We apply the active filament theory to study the main design principles that govern the configuration space of the elephant trunk: slenderness, tapering, and helicity. First, we consider a single longitudinal muscular bundle. Upon activation, the filament curls to minimize its elastic energy with dimensionless curvature $L\kappa$, $\kappa = \sqrt{\hat{u}_1^2 + \hat{u}_2^2}/\hat{\zeta}$, which extends Timoshenko's result to large deformations. In Fig. 3(a), we show that slenderness has a significant effect on the deformation. Indeed, by varying the ratio S_r of filament length L to the outer radius R_0, the same muscular activation will yield a larger curvature for filaments with a larger slenderness. This is a natural consequence of the scaling of the second moment of area of the filament's cross section as $\sim 1/S_r^4$, which dominates the less pronounced effect of the decreased fiber activation area for more slender filaments. Figure 3(a) further shows that, for sufficiently small fiber magnitudes ($|\gamma| < 1$), the dimensionless curvature $L\kappa$ is an approximately linear function of the activation in the entirety of the evaluated slenderness range $S_r \in [5, 20]$.

Second, the geometry of the elephant trunk is highly tapered, with a larger cross-sectional radius at the proximal end and increasingly smaller radii toward the distal end, effectively inducing a gradually varying slenderness. For uniform activations in a longitudinal muscle, the local curvature of the trunk increases with the decreasing trunk radius. The larger the decrease in radius the larger the increase in curvature, as demonstrated in Fig. 3(b) by the increase in maximal curvature $L\kappa_{\max}$ with the increasing tapering angle ϕ. In the physiological range of tapering angles $\phi \in [5°, 6°]$ (structures III and IV), we observe the typical curling motion that the elephants use to wrap their trunks around objects.

Third, the elephant trunk contains helical muscle fibers that we model through two opposite helical fibers. In addition to creating curvature, a single helical fiber bundle can generate torsion. Combining the effect of two identical helical fibers, but of opposite handedness, cancels the torsional contribution and creates pure bending of the filament [23], as shown in Fig. 3(c). An increase in the fiber revolution Ω results in larger maximal curvature and increased variability in the bending curvature. We

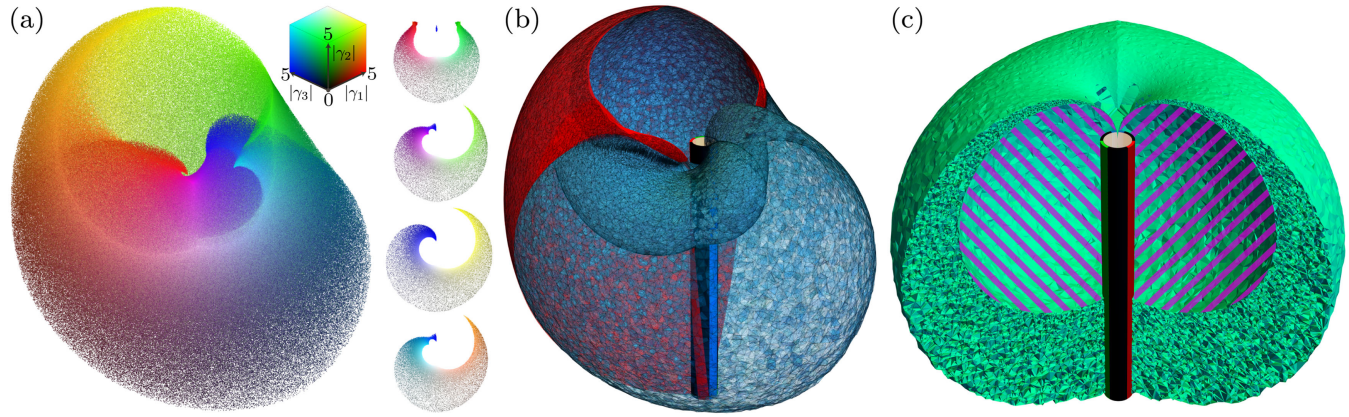

FIG. 4. Reachability cloud for a minimal elephant trunk design with three actuators. (a) The point cloud consists of 2×10^6 points, RGB-coded by activation magnitude within the range $\gamma_1, \gamma_2, \gamma_3 \in [-5, 0]$ (red, green, and blue, respectively). (b) A design with only two helical actuators (shown in red) restricts the reachability cloud to a 2D surface region compared to 3D cloud of the minimal design (in blue). (c) Similarly, a design with three longitudinal actuators has a smaller reachability cloud with a large interior unreachable region.

define $\Omega = (L/R_0)\tan\alpha$ to quantify the total fiber revolution throughout the filament for a given helical angle α; see SM for details. The influence of Ω on the resulting deformation is similar to the effect of varying the tapering angle ϕ: the rate of increase of curvature along Z is amplified by increasing either Ω or ϕ, which might be responsible for generating the curling deformations commonly observed in elephant trunks motions.

Minimal elephant trunk-inspired design.—Our study in Fig. 3 suggests that a single muscular bundle or two opposing helical bundles can generate a variety of deformation modes. By combining these modes, we can create a minimal design of a tubular structure made up of one longitudinal and two helical fibers. The longitudinal fiber generates pure curvature, as inspired by the massive upper muscle group in the elephant trunk; see Fig. 1. The two symmetrically arranged helical fibers generate either twist, torsion, or curvature depending on their relative activation magnitudes; see Fig. 4 and the design parameters in the SM.

To quantify the performance of this design, we created a comprehensive three-dimensional reachability point cloud in Fig. 4(a) to illustrate the space of end points accessible by the trunk by randomly sampling muscular activations. Notably, the reachability cloud consists of 2×10^6 points and takes less than 1 min to compute on a standard desktop computer, at a rate of roughly 100 000 configurations per second thanks to the semianalytical nature of the model and unlike traditional finite-element code.

The resulting cloud spans an extensive three-dimensional space within the entire 360° arc around the longitudinal axis of the initial configuration. Our minimal trunk design can reach points to the front, back, right, and left of the initial configuration, as well as anywhere in between these regions. For comparison, the trunk of an Asian elephant can generate compressive strains up to 33% [24], which corresponds to a stretch of 0.67 and an activation of $\gamma \approx -3.33$ in our minimal design. Importantly, a tight concave hull of the reachability cloud with a normalized volume $\tilde{V}_{\text{cloud}} = V_{\text{cloud}}/L^3 \approx 0.85$ amounts to about 74% of the convex hull with $\tilde{V}_{\text{conv}} \approx 1.14$, which implies that only 26% of the conservative volume bounded by the cloud is inaccessible by the design. Comparison with other designs containing either two helical actuators or three longitudinal ones shows in Figs. 4(b) and 4(c) that our minimal design is vastly superior in terms of reachability. Specifically, removing the blue longitudinal actuator reduces the reachability cloud to a 2D surface [Fig. 4(b)]. Replacing the helical actuators with longitudinal ones decreases the cloud volume by 14% to $\tilde{V}_{\text{cloud}} \approx 0.73$ due to a large inaccessible void created by the removal of helical fibers, amounting to almost 42% of the new convex hull [Fig. 4(c)]. Indeed, the torsional modes activated by the helical fibers empower the design to not only reach a larger space, but also perform a variety of complex motions, including avoiding obstacles or grasping and rotating objects through curling, a common motion performed by elephant trunks when manipulating branches of trees.

Experimental validation.—We validate our predicted deformation patterns with experimental deformations of a soft slender structure actuated by liquid crystal elastomer fibers. Briefly, we created an inactive acrylate polymer-based slender cylinder via molding. Three active liquid crystal elastomer fibers were fabricated through 3D printing for mesogen alignment. Before curing, we embedded a coiled copper wire in each of the fibers to enable active contraction through Joule heating. We then cured the fibers with ultraviolet light to fix the mesogen alignment and lock the wire in place. Finally, we bonded the resulting fibers to the elastic cylinder, giving us the complete experimental model.

Figure 5 shows a direct comparison of five representative deformation types for the activation of (i) the single

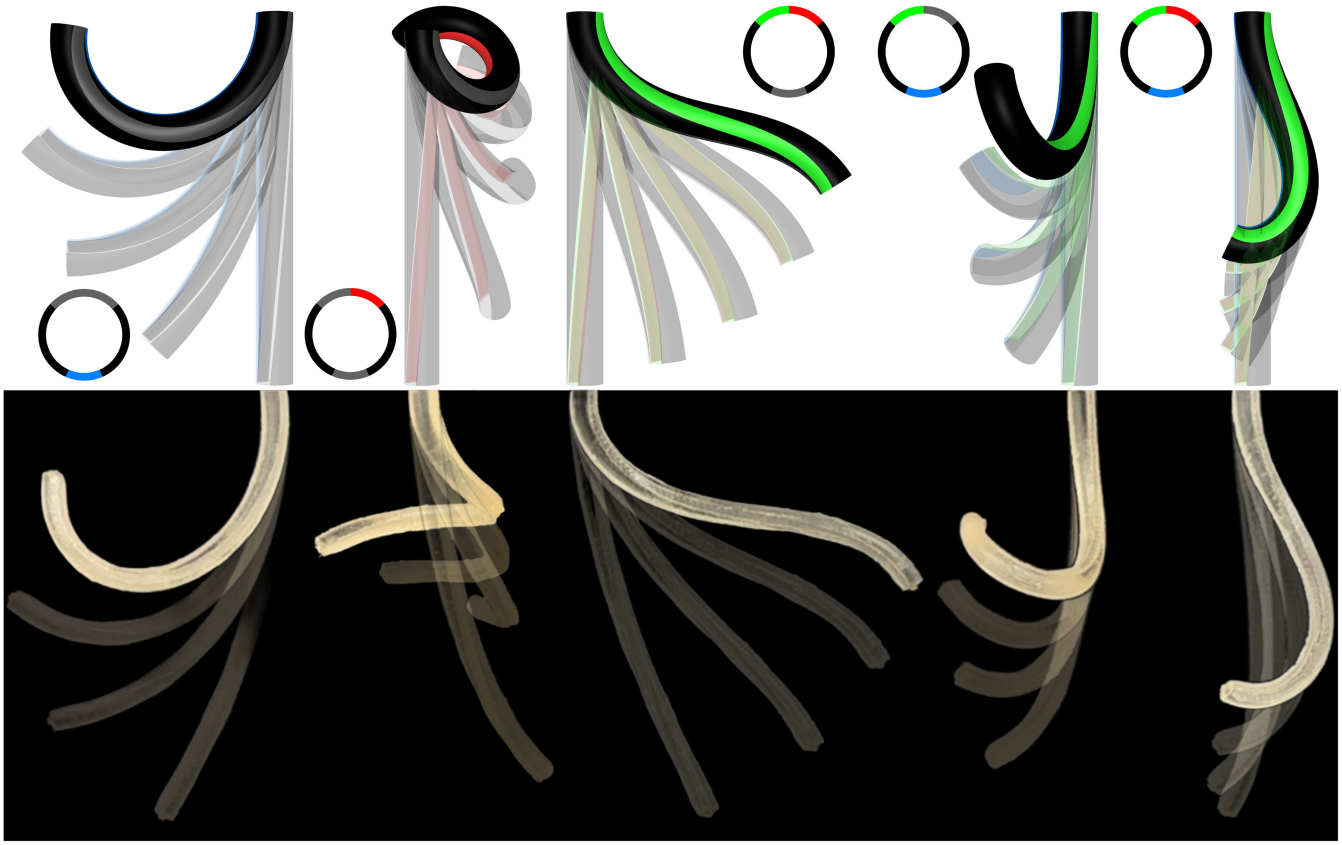

FIG. 5. Experimental validation of predicted deformation patterns. Activation of the single longitudinal, a single helical, both helical, a pair of longitudinal and helical, and all fibers, from left to right. Gray color indicates no activation in a given fiber. The predicted deformation patterns (top) agree with the experimental deformations of a soft slender structure activated by liquid-crystal elastomer fibers (bottom).

longitudinal fiber, (ii) a single helical fiber, (iii) both helical fibers, (iv) a pair of longitudinal and helical fibers, and (v) all three fibers, from left to right. The model predictions in Fig. 5 include the effects of gravity (see SM). The five configurations in Fig. 5 illustrate the richness of possible deformation types: configuration (i) exhibits *pure bending* achieved by the longitudinal actuator only; configuration (ii) exhibits high *torsion* through activation of one of the helical actuators; configuration (iii) exhibits *pure bending*, with the bending direction changing halfway; configuration (iv) represents a *combination of bending and torsion* that generates an out-of-plane motion through the interplay of the longitudinal and helical actuators; finally, configuration (v) shows the torsion cancellation effect in configuration (iii), but the longitudinal fiber induces *localized bending* at the distal end of the design.

The simulated configurations agree with the experimental deformation patterns, which supports the utility of our parametric studies and reachability considerations. Further, we emphasize that the five deformation cases shown in Fig. 5 are a small subset of all achievable deformation types, given that the selected cases merely correspond to five fiber subsets and five sets of activation magnitudes. The reachability cloud in Fig. 4 is a consequence of an otherwise much richer configuration space generated by an exhaustive sweep through all activation combinations in the three fibers.

Elephant trunk motions.—As a final step, we show in the SM that our minimal design can mimic the physiological deformations in an elephant trunk motion recorded by Dagenais *et al.* [3] using motion capture technology.

Conclusion.—Unlike traditional robotic arms with finite degrees of freedom, soft structures like the elephant trunk or the octopus arm have infinitely many, hence creating "a body of pure possibility" according to the philosopher Peter Godfrey [25]. This universe of possibilities is made possible through fundamental physical mechanisms coupling geometry to mechanics, amplified by the *slenderness* of the structure and the *softness* of matter. While curvature generation in a one-dimensional structure is easy to understand and create through longitudinal contraction, the creation of twist and torsion requires dedicated helical fibers. To create both left- and right-handed structures, the design requires two helical bundles with opposite handedness. Hence, the simplest design is a three-actuator architecture inspired by the elephant trunk. Here, we

demonstrate, analytically, computationally, and experimentally, that this minimal design is sufficient to reach a large portion of space. Further, the large range of deformation types empowered by this minimal design suggests that it could play an important role in motion planning tasks. Finally, the comparison of simulated deformations to the biological motions reinforces the minimality and versatility of the bio-inspired design in that only three independent fibers can reproduce a large set of motion archetypes accessible by the anatomically complex elephant trunk.

This letter has been funded by EPSRC Grant No. EP R020205 and the NSF Grant No. CMMI 2318188. B. K., E. K., D. M., and A. G. designed the study and developed the theory, B. K. performed the computations, and S. L. and R. Z. designed the actuators and performed the experiments. All authors analyzed the data, discussed the results, and wrote the Letter.

*Corresponding author: goriely@maths.ox.ac.uk

[1] S. P. Timoshenko, J. Opt. Soc. Am. **11**, 233 (1925).
[2] D. E. Moulton, H. Oliveri, and A. Goriely, Proc. Natl. Acad. Sci. U.S.A. **117**, 32226 (2020).
[3] P. Dagenais, S. Hensman, V. Haechler, and M. C. Milinkovitch, Curr. Biol. **31**, 4727 (2021).
[4] L. V. Kaufmann, U. Schneeweiß, E. Maier, T. Hildebrandt, and M. Brecht, Sci. Adv. **8**, eabq2789 (2022).
[5] L. Purkart, J. M. Tuff, M. Shah, L. V. Kaufmann, C. Altringer, E. Maier, U. Schneeweiß, E. Tunckol, L. Eigen, S. Holtze *et al.*, Curr. Biol. **32**, 904 (2022).
[6] L. L. Longren, L. Eigen, A. Shubitidze, O. Lieschnegg, D. Baum, J. A. Nyakatura, T. Hildebrandt, and M. Brecht, Curr. Biol. **33**, 4173 (2023).
[7] J. E. V. Boas and S. Paulli, *The Elephant's Head: Studies in the Comparative Anatomy of the Organs of the Head of the Indian Elephant and Other Mammals* (Gustav Fischer, 1908).
[8] G. Cuvier and C. L. Laurillard, *Anatomie comparée, recueil de planches de myologie dessinées par Cuvier... ou Laurillard, publié sous les auspices de ministre de l'instruction par Laurillard et Mercier:...* (Dusacy, 1850).
[9] J. Wu, Y. Zhao, Y. Zhang, D. Shumate, S. Braccini Slade, S. V. Franklin, and D. L. Hu, J. R. Soc. Interface **15**, 20180377 (2018).
[10] A. K. Schulz, M. Boyle, C. Boyle, S. Sordilla, C. Rincon, S. Hooper, C. Aubuchon, J. S. Reidenberg, C. Higgins, and D. L. Hu, Proc. Natl. Acad. Sci. U.S.A. **119**, e2122563119 (2022).
[11] Q. Guan, J. Sun, Y. Liu, N. M. Wereley, and J. Leng, Soft Rob. **7**, 597 (2020).
[12] D. Trivedi, C. D. Rahn, W. M. Kier, and I. D. Walker, Appl. Bionics Biomech. **5**, 99 (2008).
[13] J. Zhang, Y. Li, Z. Kan, Q. Yuan, H. Rajabi, Z. Wu, H. Peng, and J. Wu, Soft Rob. **10**, 636 (2023).
[14] B. Kaczmarski, D. E. Moulton, A. Goriely, and E. Kuhl, Comput. Methods Appl. Mech. Eng. **408**, 115939 (2023).
[15] B. Kaczmarski, A. Goriely, E. Kuhl, and D. E. Moulton, IEEE Rob. Autom. Lett. **8**, 936 (2023).
[16] B. Kaczmarski, D. E. Moulton, E. Kuhl, and A. Goriely, J. Mech. Phys. Solids **164**, 104918 (2022).
[17] D. E. Moulton, T. Lessinnes, and A. Goriely, J. Mech. Phys. Solids **45**, 104022 (2020).
[18] A. Goriely, *The Mathematics and Mechanics of Biological Growth* (Springer, New York, 2017).
[19] See Supplemental Material, which includes Refs. [20–22], at http://link.aps.org/supplemental/10.1103/PhysRevLett.132.248402 for a detailed description of fibrillar activation, special solutions and material properties used in the simulations, specific parameters of the minimal design, details of the reachability cloud computation, experimental methods, and a comparison of the minimal design deformations with real elephant trunk motions.
[20] J. H. Verner, Numer. Algorithms **53**, 383 (2010).
[21] H. Edelsbrunner, D. Kirkpatrick, and R. Seidel, IEEE Trans. Inf. Theory **29**, 551 (1983).
[22] D. E. Moulton, T. Lessinnes, and A. Goriely, J. Mech. Phys. Solids **61**, 398 (2013).
[23] A. Goriely and M. Tabor, Proc. R. Soc. A **469** (2013).
[24] J. F. Wilson, U. Mahajan, S. A. Wainwright, and L. J. Croner, J. Biomech. Eng. **113**, 79 (1991).
[25] P. Godfrey-Smith, Other Minds: the Octopus, the Sea, and the Deep Origins of Consciousness (Farrar, Straus and Giroux, New York, 2016).